

Photocatalytic Conversion of CO₂ to Hydrocarbon Fuels via Plasmon-Enhanced Absorption and Metallic Interband Transitions

Wenbo Hou,[†] Wei Hsuan Hung,[§] Prathamesh Pavaskar,[‡] Alain Goeppert,[†] Mehmet Aykol,[‡] and Stephen B. Cronin^{*,†,‡}

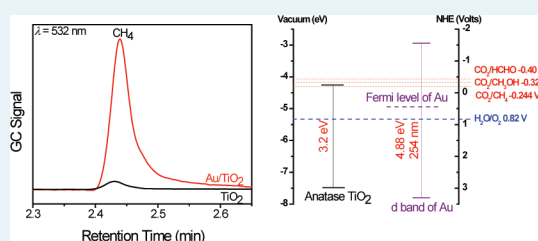
[†]Department of Chemistry, [‡]Department of Electrical Engineering, and [§]Department of Materials Science, University of Southern California, Los Angeles, California 90089, United States

Supporting Information

ABSTRACT: A systematic study of the mechanisms of Au nanoparticle/TiO₂-catalyzed photoreduction of CO₂ and water vapor is carried out over a wide range of wavelengths. When the photon energy matches the plasmon resonance of the Au nanoparticles (free carrier absorption), which is in the visible range (532 nm), we observe a 24-fold enhancement in the photocatalytic activity because of the intense local electromagnetic fields created by the surface plasmons of the Au nanoparticles. These intense electromagnetic fields enhance sub-bandgap absorption in the TiO₂, thereby enhancing the photocatalytic activity in the visible range.

When the photon energy is high enough to excite d band electronic transitions in the Au, in the UV range (254 nm), a different mechanism occurs resulting in the production of additional reaction products, including C₂H₆, CH₃OH, and HCHO. This occurs because the energy of the d band excited electrons lies above the redox potentials of the additional reaction products CO₂/C₂H₆, CO₂/CH₃OH, and CO₂/HCHO. We model the plasmon excitation at the Au nanoparticle-TiO₂ interface using finite difference time domain (FDTD) simulations, which provides a rigorous analysis of the electric fields and charge at the Au nanoparticle-TiO₂ interface.

KEYWORDS: photocatalytic, photocatalysis, plasmon, plasmonic, interband transition, CO₂, hydrocarbon fuels



INTRODUCTION

Photocatalytic conversion of carbon dioxide into hydrocarbons is of great interest for its potential to convert an abundant greenhouse gas to useful hydrocarbon fuels. In 1979, Inoue et al. first demonstrated the photoelectrocatalytic reduction of aqueous carbon dioxide to produce formic acid, formaldehyde, methyl alcohol, and methane using semiconducting photocatalytic powders, including TiO₂, ZnO, CdS, GaP, SiC, and WO₃.¹ In addition, Halmann reported formic acid production from aqueous CO₂ at the p-type GaP photocathode in an electrochemical photocell² and oxide semiconductors in a photochemical solar collector.³ Hemminger and co-workers demonstrated photosynthetic reduction of carbon dioxide in water vapor to form methane on SrTiO₃ crystalline surfaces without any externally applied potential and in the absence of a liquid electrolyte.⁴

TiO₂ is one of the most promising photocatalysts for carbon dioxide reduction; however, it does not absorb light in the visible region of the electromagnetic spectrum. Because of TiO₂'s short wavelength cutoff, only a small fraction of solar photons (~4%) can be used to drive this photocatalyst. The resulting low photocatalytic yield of TiO₂ is perhaps its main disadvantage for the photocatalytic conversion of carbon dioxide into hydrocarbons. Several attempts have been made to increase its yield.⁵ For example, copper-,^{5–7} copper oxide-,^{8,9} silver-,^{7,10} and ruthenium dioxide-doped¹¹ TiO₂ have resulted in increased yields. Previously, our group and several others have reported plasmon

resonant enhancement of dye photodegradation,¹² oxidation of CO¹³ and organic compounds,¹⁴ and photoelectrochemical reactions.^{15,16} However, the mechanism for this increased photocatalytic activity is controversial. Tatsuma's group and others treat the plasmon excitation in the metals as having an energy separation between the electrons and holes, which enables electron transfer from the Au nanoparticles to the adjacent TiO₂.^{14–16} However, surface plasmons consist of the collective oscillation of charge bound to the Au surface, and therefore have no highest occupied molecular orbital (HOMO) to lowest unoccupied molecular orbital (LUMO) or valence band-conduction band energy separation associated with them. It is well-known that a Schottky barrier is formed at metal-semiconductor junctions. In this paper, we provide a rigorous analysis of this charge transfer process by calculating the electron transfer from the plasmon excitation in the Au nanoparticle to the TiO₂ semiconductor using the electric potentials calculated from numerical electromagnetic simulations together with the ideal diode equation for a Au/TiO₂ Schottky junction.

Noble metal nanoparticles combined with semiconductors have been widely studied for improved charge separation of photogenerated electron–hole pairs, thus enhancing the overall photocatalysis of semiconductors under UV illumination.^{17–22}

Received: March 14, 2011

Revised: June 27, 2011

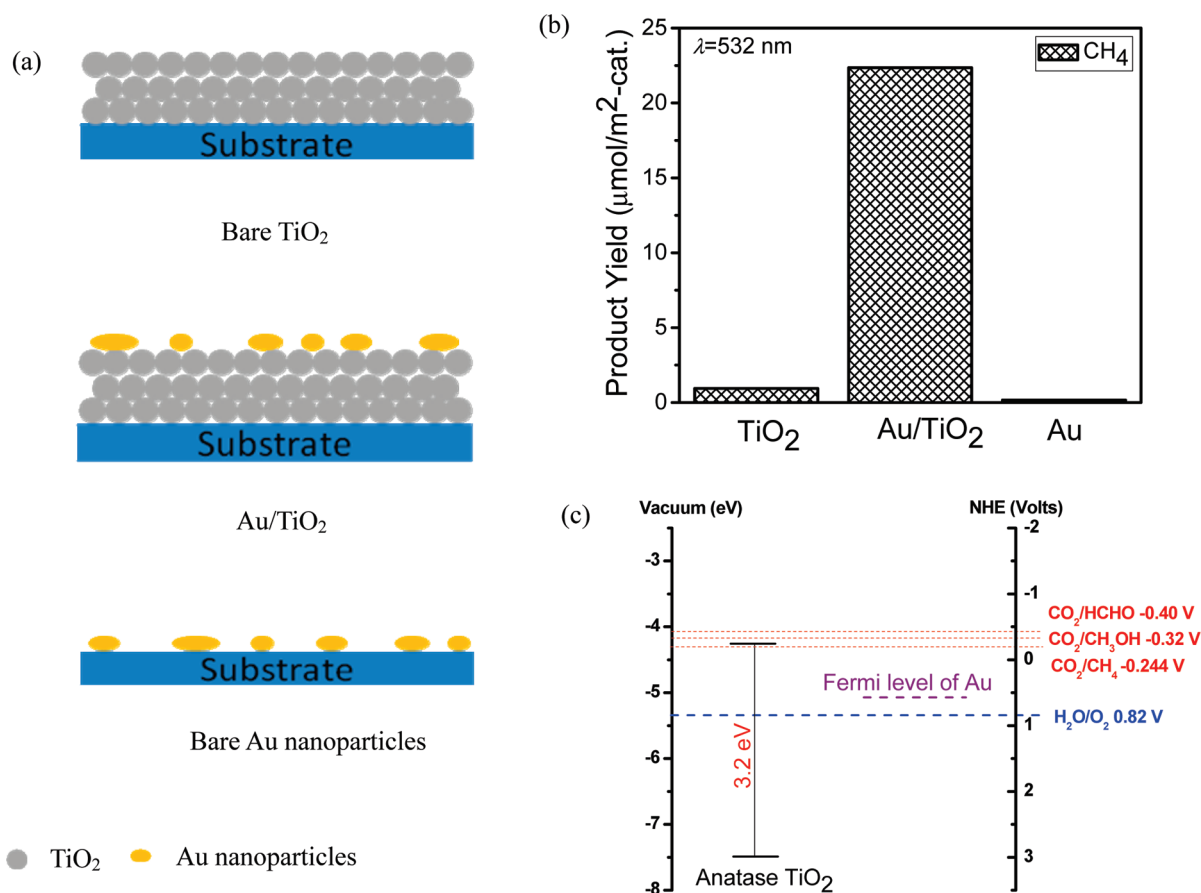


Figure 1. (a) Schematic diagrams of three types of photocatalysts. (b) Photocatalytic product yields (after 15 h of visible irradiation) on three different catalytic surfaces. (c) Energy band alignment of anatase TiO₂, Au, and the relevant redox potentials of CO₂ and H₂O under visible illumination.

Noble metal nanoparticles alone are also potential photocatalysts, since they also can absorb UV light via interband transitions.²³ However, the photocatalytic activity of noble metal nanoparticles themselves has not been acknowledged as significant. It is worth mentioning that Haruta and co-workers have previously carried out extensive studies of Au nanoparticles on metal oxide surfaces.^{24–28} In their work, Au nanoparticle/metal oxide composites were used to catalyze thermally driven oxidation reactions at low temperatures, rather than photocatalytic processes. Zhu et al. have observed photocatalytically driven dye photodecomposition, phenol degradation, and benzyl alcohol oxidation under UV illumination arising from the electronic interband transitions in Ag.²³ Under visible illumination, however, no phenol degradation or benzyl alcohol oxidation was observed. Photodecomposition of organic dye molecules is observed under visible light, and was attributed to surface plasmon resonance. However, the details of this mechanism were not discussed, whether it was a charge-, thermal-, or field-mediated process. Besides Ag, Au also has interband electronic transitions in the UV range,^{29–31} and thus Au nanoparticles themselves can also contribute to the photocatalytic activity of metal/semiconductor composites under UV radiation.

In this paper, we study the mechanisms of Au nanoparticle/TiO₂-catalyzed photoreduction of aqueous CO₂ under four different excitation wavelengths (two in the visible range and two in the UV range), which enables us to separate processes associated with the plasmon resonance (visible range) from

those associated with electronic transitions in the Au itself (UV range). The mechanisms for increased photocatalytic activity are studied systematically by monitoring various reaction products, which have different reduction potentials. We model the plasmon excitation at the Au nanoparticle-TiO₂ interface using finite difference time domain (FDTD) simulations, which provides a rigorous analysis of the electric fields and charge at the Au nanoparticle-TiO₂ interface. Our interband transition hypothesis/model provides an alternative explanation for the enhancement role of noble metal nanoparticles in TiO₂ photocatalysis purely based on the relative energies of the electrons and holes in the solid materials with respect to the redox potentials of the reaction products.

EXPERIMENTAL SECTION

In this work, three basic sample types are fabricated and characterized: (1) bare TiO₂, (2) Au nanoparticles deposited on top of TiO₂, and (3) bare Au nanoparticles, as depicted in Figure 1a. Anatase titania thin films are prepared in our lab by the sol-gel process and follow the general recipe of acid catalyzing dilute titanium ethoxide in ethanol.³² The solution is then mixed with surfactant (P123) and stirred for several hours until a sol forms. Substrates of glass or quartz are spin-coated to achieve the desired film thickness of 400 nm. The substrates are then positioned horizontally and dried at room temperature in air for 24 h, thereby allowing most of the solvents and hydrochloric

acid to evaporate and the surfactant to self-organize. The dried films are then annealed at 400 °C in air for 4 h to improve their crystallinity and drive off any remaining solvents and surfactant. Raman and XRD spectra of the resulting TiO₂ are given in Supporting Information, Figure S1, which shows that anatase TiO₂ is obtained. A thin film of gold is deposited on the TiO₂ surface in vacuum using electron beam evaporation, while the film thickness is monitored with a crystal oscillator. A 5 nm deposition of gold is not thick enough to form a continuous film and, instead, produces an island-like morphology that is known to be strongly plasmonic.^{33,34} A high resolution transmission electron microscope (TEM) image of a 5 nm Au film is shown in Figure 4a. Subsequent annealing of this island-like film at 400 °C in air for 1 h produces more spherical Au nanoparticles, as shown in Supporting Information, Figure S2. Thin Au evaporated films (~5 nm) are known to form island-like growth, which serve as good substrates for surface enhanced Raman spectroscopy (SERS) and other plasmonic phenomena.^{34–37} To make bare Au nanoparticles on an inactive support, a gold film with a nominal thickness of 5 nm is evaporated on glass.

Absorption spectra of the bare TiO₂ and Au nanoparticle/TiO₂ films are recorded on a Perkin-Elmer Lambda 950 UV/vis/NIR spectrophotometer with an integrating sphere detector. The photocatalytic reduction of CO₂ and H₂O are carried out in a sealed 51.6 mL stainless steel reactor with a quartz window for the three basic sample types described above. The photocatalytic films are placed on the catalyst holder, which is on the bottom of the reactor. A schematic diagram of the experimental setup is shown in Supporting Information, Figure S3. The reactor is first purged with CO₂ saturated water vapor for 1 h before closing the system. The reactor is then illuminated with either UV light (254 nm 20 mW/cm² or 365 nm 20 mW/cm² UV lamp) or visible light (532 nm 350 mW/cm² green laser) for 15 h at 75 °C. The irradiated surface area is limited by the surface area of the photocatalysts (10 cm²). Reaction products are analyzed using a Varian gas chromatograph (GC) equipped with TCD (with a detection limit of 100 ng for CO₂) and FID (with a detection limit of 50 pg for small organic molecules) detectors. The GC is calibrated by a series of gas samples with known amounts of CH₄, CH₃OH, HCHO, and C₂H₆. A 300 μL portion of gas (products and unreacted reagents) is sampled after 15 h of illumination for each reaction. Since only 300 μL of unreacted reagents and products are sampled and tested using GC, the yields are calculated by normalizing to the full volume of the reactor (51.6 mL).

RESULTS

Figure 1b shows the product yields of the photoreduction of aqueous CO₂ expressed per 1 m² of catalyst surface area after 15 h visible (532 nm laser) illumination. Here, methane is the only product detected by the GC for the three basic sample types, bare sol–gel TiO₂, Au nanoparticle/TiO₂, and bare Au nanoparticles. These reactions can be understood by comparing the conduction and valence band energies of TiO₂ with the reduction potentials of CO₂ for the three reduction products CH₄, HCHO, and CH₃OH, as shown in Figure 1c.^{1,4} Since the conduction band of TiO₂ lies above the reduction potential of CO₂/CH₄,³⁸ it is energetically favorable for electrons from the conduction band of TiO₂ to transfer to CO₂ to initiate the reduction of CO₂ with H₂O producing CH₄.³⁹ Methane is the only favorable product

since the reduction potentials of CO₂/HCHO and CO₂/CH₃OH lie above the conduction band of TiO₂.^{1,4} For the bare TiO₂-catalyzed reduction, only a small amount of methane is detected by GC since the energy of the 532 nm wavelength light (2.41 eV) is significantly lower than the bandgap of TiO₂ (3.2 eV). The yield is finite, yet small (0.93 μmol/m²-cat.), because of electronic transitions excited to and from defect states in the bandgap of TiO₂. On the other hand, the yield of Au nanoparticle/TiO₂-catalyzed reduction is 22.4 μmol/m²-cat., a 24-fold enhancement over the bare constituent materials. This enhancement in sub-bandgap absorption/photocatalysis is consistent with our previous work,^{12,40} wherein the intense local fields produced by the plasmonic nanoparticles couple light very effectively from the far-field to the near-field, short-lived defect states at the TiO₂ surface. As a control experiment, bare Au nanoparticles without TiO₂ were also tested and found to exhibit a negligible photocatalytic yield (Figure 1b), indicating the importance of the TiO₂ surface in this catalytic process. This result agrees well with our previous studies.^{12,40} Under visible illumination, electron–hole pairs are generated by the sub-bandgap transitions in TiO₂, instead of in Au. Plasmon-excited electrons in Au nanoparticles are not able to transfer to the either TiO₂ or the reagents.

The UV–vis absorption spectrum taken for a bare TiO₂ film prepared by the sol–gel method (as shown in Supporting Information, Figure S4) shows transparency for wavelengths above 387 nm, which corresponds to the bandgap of anatase TiO₂ (3.2 eV). In our previous work involving anodic TiO₂ (ATO),⁴⁰ however, this defect concentration was much higher because of N- and F-impurities produced during the anodization process,⁴¹ which resulted in an obvious UV–vis absorption. While the UV–vis absorption spectra of the bare sol–gel TiO₂ shows no apparent absorption below the bandgap, finite sub-bandgap absorption does occur because of a small concentration of defect states in the bandgap due to a Ti⁴⁺ stoichiometry deficiency,⁴² thus, enabling electron–hole pair generation at 532 nm. In our previous water-splitting photocatalysis work, no photocurrent was observed for the sol–gel prepared TiO₂ because of the high resistance of the sol–gel film, which decreases the water splitting photocurrent. This high resistance, however, does not affect the CH₄ photocatalytic reaction, since there is no electrochemical circuit. In this present work, ATO was also tested, and was found to produce CH₄ under visible (532 nm) illumination (19.7 μmol/m²-cat.). Furthermore, photocatalytic enhancement by 17% was observed with the addition of gold nanoparticles (5 nm film) on the ATO (23.1 μmol/m²-cat.).

To understand the mechanism of enhanced hydrocarbon production by the photoreduction of CO₂ and H₂O, we also characterized this reaction under UV irradiation. Figure 2 shows the product yields of the photoreduction of aqueous CO₂ expressed per 1 m² of catalyst surface area after 15 h UV (254 nm mercury lamp) illumination. For the bare TiO₂ catalyst, methane is the only product detected by GC. However, we observe additional reaction products, including ethane, formaldehyde, and methanol, for the Au nanoparticle/TiO₂-catalyzed reactions. Interestingly, we also observe these same four reaction products upon illumination of bare Au nanoparticles deposited on glass, indicating that the reaction is now taking place on the Au surface.

Again, we are able to understand these results by comparing the conduction and valence band energies of TiO₂ and Au with

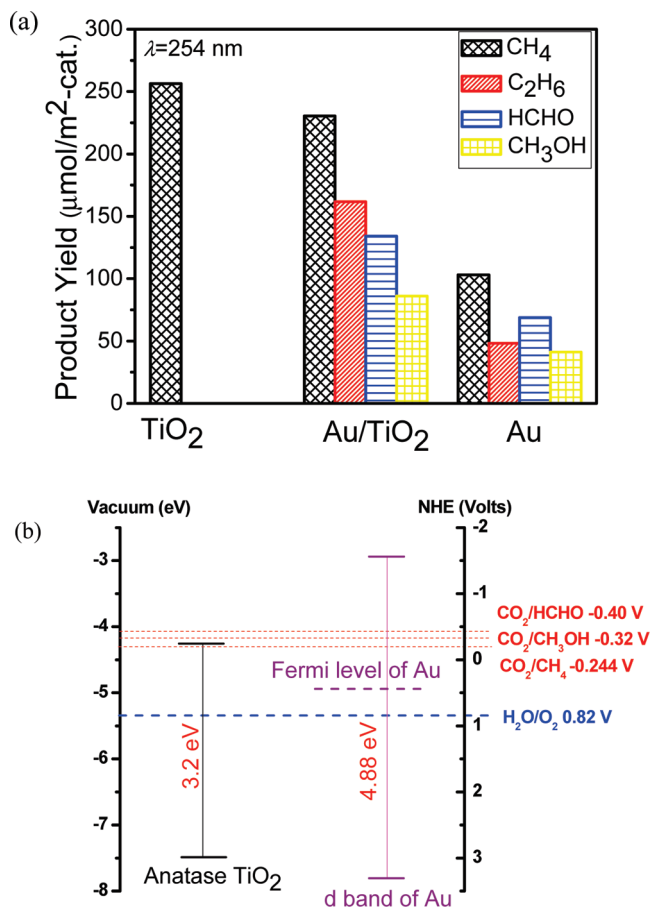


Figure 2. (a) Photocatalytic product yields (after 15 h of 254 nm UV irradiation) on three different catalytic surfaces. (b) Energy band alignment of anatase TiO₂, Au, and the relevant redox potentials of CO₂ and H₂O under 254 nm UV illumination.

the reduction potentials of CO₂ for the reduction products CH₄, HCHO, and CH₃OH, as shown in Figure 2b. While the conduction band of TiO₂ lies above the reduction potential of CO₂/CH₄, it is below the reduction potentials of CO₂/HCHO and CO₂/CH₃OH. As a result, methane is the only product for the bare TiO₂-catalyzed reaction. Metals are often thought of as simply having electronic states filled up to a Fermi energy corresponding to the work function of the metal. However, like any crystalline material, metals have higher lying electron bands that are normally unoccupied.^{31,43} In noble metals, the d-electron bands lie below the Fermi level (E_F). Interband transitions from the d-band to an empty sp state above E_F can occur during the optical absorption process.⁴⁴ In Au, the first interband excitation occurs at the X-point in the Brillouin zone, at an energy of 2.5 eV.^{45,46} The energy of the 254 nm wavelength light (4.88 eV) exceeds the minimum energy required for interband transitions in Au and therefore is able to excite electrons from its d band to the conduction band, which lies above the conduction band of TiO₂ and the reduction potentials of CO₂/CH₄, CO₂/CH₃OH, and CO₂/HCHO, as shown in Figure 2b. These highly energetic electrons are then able to drive all of these products of the reduction of CO₂ and H₂O. Thus, methane, ethane, formaldehyde, and methanol are observed in the Au nanoparticle/TiO₂- and bare Au-catalyzed reactions under 254 nm UV illumination. In this process, both redox half reactions occur at the Au surface.

The excited electrons are given to CO₂ to form reduction products, while the holes drive the other half reaction to form O₂. The half-reaction equations for these redox reactions are given in the Supporting Information. X-ray photoelectron spectra (XPS) (Supporting Information, Figure S5) show the binding energies of Au_{4f7/2} in the Au/TiO₂ sample at 84.3 and 84.2 eV before and after the reaction, which are significantly different from Au⁺_{4f7/2} (85.2 eV) and Au³⁺_{4f7/2} (86.7 eV) but similar to Au⁰_{4f7/2} (84.0 eV).⁴⁷ If the reduction half-reactions occur on the Au surface and the oxidation half-reaction on the TiO₂ surface, the Au should lose electrons and leave holes on its surface. This would shift the electron binding energies of Au to higher energies, corresponding to oxidized states after the reaction. However, we observe no change in the XPS binding energies, indicating that the oxidation state of the Au surface remains the same before and after the reaction. Therefore, this confirms that both half reactions occur on the Au surface. The slight enhancement (~2×) in the product yields of Au/TiO₂ over bare Au likely arises from charge transfer from the highly energetic excited electrons in the Au to the adjacent TiO₂, and from charge generated by the direct absorption of UV light in the TiO₂. In this scenario, reactions take place on both the TiO₂ and Au surfaces. We would like to point out that at 254 nm, which is significantly above the plasmon resonance of the gold, there is no local field enhancement produced by the Au nanoparticles. The catalytic activity of a 30 nm evaporated Au continuous thin film deposited on glass without TiO₂ was also tested under UV illumination and was found to produce the same yields for methane, ethane, formaldehyde, and methanol as the 5 nm Au thin film without TiO₂. This photocatalytic process under 254 nm UV illumination is driven solely by the interband transitions in Au, which do not require a nanometric morphology. A 5 nm film of gold is not thick enough to form a continuous film. Instead, this produces a film of gold islands with an average size of approximately 20 nm. These films are known to be strongly plasmonic, and have been utilized for surface enhanced Raman spectroscopy (SERS) for many years.^{33,34} The island-like morphology of a 5 nm Au film is shown in the transmission electron microscope (TEM) image of Figure 4a. The 30 nm Au thin film forms a continuous bulk Au layer, not Au nanoparticles, and serves as a control sample to separate and identify effects associated with bulk Au (i.e., interband transitions) rather than plasmon resonance.

Several earlier studies by Gupta's group showed that different photo-oxidation products were caused by distinct free-radicals or ion-radical species formed at TiO₂ surfaces and Au/TiO₂ interfaces under different incident radiation energies.^{48,49} However, here, we observe different products with different catalysts. In addition, we expect the effects of localized plasmonic heating to be negligibly small in this system. Previously, we observed plasmonic heating for incident light intensities above 1.4×10^6 W/cm².⁵⁰ In the work presented here, the incident light intensity is 0.35 W/cm², which is 7 orders of magnitude below that which is expected to produce significant heating. Unfortunately, we are unable to identify radical species in our experimental setup; however, our results can be understood purely based on the relative energies of the electrons and holes in the solid materials with respect to the redox potentials of the reaction products. This model does not depend on or give information about intermediate radical species, but provides an alternative framework with which to understand the Au/TiO₂ catalytic system.

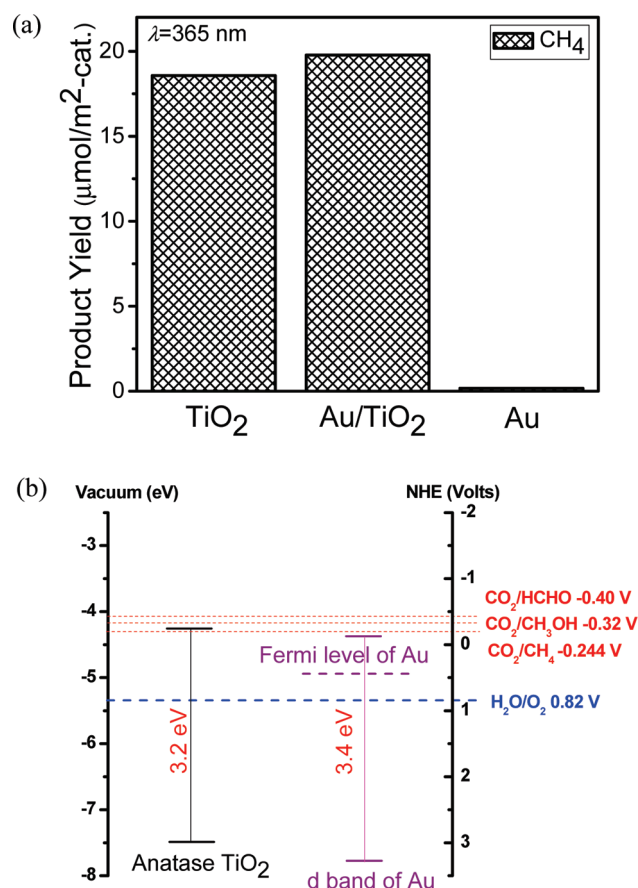


Figure 3. (a) Photocatalytic product yields (after 15 h of 365 nm UV irradiation) on three different catalytic surfaces. (b) Energy band alignment of anatase TiO₂, Au, and the relevant redox potentials of CO₂ and H₂O under 365 nm UV illumination.

The interband transition mechanism proposed under UV illumination is not only applicable to gold-catalyzed photoreactions. In addition, the catalytic activities of a 5 nm Pt thin film deposited on glass and a Cu foil were also tested. The yields for methane, ethane, formaldehyde, and methanol of the 5 nm Pt thin film and Cu foil are similar to that of the 5 nm Au thin film, as shown in Supporting Information, Figure S6.

We also characterized this reaction under 365 nm UV illumination for the same three basic sample types (Figure 3). Under 365 nm UV illumination, no products were formed for the 5 nm Au thin film alone and only methane was formed for TiO₂ and Au nanoparticle/TiO₂-catalyzed reactions. The reason no products are formed on the bare Au nanoparticles surface is that the energy of the 365 nm light (3.4 eV) is not high enough to excite electrons beyond the redox potentials of the CO₂/CH₄, CO₂/HCHO, CO₂/CH₃OH reduction potentials, as shown in Figure 3b. The electrons excited by interband transitions in the Au also lie below the conduction band of TiO₂, and, therefore, no electrons are transferred from the Au to the TiO₂. These results under UV illumination further confirm that the plasmonic enhancement of photocatalysis under visible illumination is a result of the strong electric fields created by the surface plasmons of the Au nanoparticles rather than direct transfer of the charge. The methane formed in the TiO₂ and Au nanoparticle/TiO₂-catalyzed reactions is due to direct absorption in the TiO₂, since the energy of the 365 nm light is above the bandgap of TiO₂. It

Table 1. Overall Quantum Efficiency (%) of Reduction of CO₂ and H₂O on TiO₂, Au, and Au/TiO₂ Catalysts under UV and Visible Irradiation

light source	TiO ₂	Au/TiO ₂	Au
UV (20 mW/cm ² , 254 nm)	8.9×10^{-3}	2.3×10^{-2}	8.8×10^{-3}
UV(20 mW/cm ² , 365 nm)	6.5×10^{-4}	6.9×10^{-4}	0
Visible (350 mW/cm ² , 532 nm)	8.8×10^{-7}	2.1×10^{-5}	0

should be noted that this 365 nm light lies above the plasmonic modes in the system; therefore, no plasmonic enhancement occurs in the Au nanoparticle-TiO₂ catalyst sample.

As another control experiment, we performed bare TiO₂ and Au/TiO₂-catalyzed photoreduction of CO₂ and H₂O under 633 nm laser irradiation, which is well below the bandgap energy of TiO₂ and the Au interband transition energy. No products were observed after 15 h irradiation. In our previous study, ATO was used as the photocatalyst instead of sol-gel TiO₂.⁴⁰ The concentration of defect states with energies below the bandgap of ATO are much larger than that in the sol-gel prepared TiO₂ (as shown in the UV-vis spectra in the Supporting Information). Therefore, no products were observed under 633 nm illumination for sol-gel samples.

The quantum efficiencies of our samples are calculated using eq 1 and are summarized in Table 1. Here, n is the number of moles of electrons required to produce one mole of reduction product from CO₂, which includes CH₄, C₂H₆, CH₃OH, and HCHO. The total photon flux irradiating the catalytic surface is determined from the incident light intensity and exposure time. For the Au/TiO₂-catalyzed reaction, the quantum efficiency is roughly equal to the sum of the quantum efficiencies of the TiO₂-catalyzed reaction and Au nanoparticle-catalyzed reaction under UV illumination. This confirms that the mechanism under UV illumination includes interband transitions in both TiO₂ and Au. The quantum efficiency under visible light irradiation is 3 orders of magnitude smaller than that under UV irradiation, since the high energy photons can drive both sub-bandgap transitions and interband transitions. Low energy photons, on the other hand, can only drive sub-bandgap transitions in TiO₂, which have absorption cross sections that are significantly smaller than interband transitions. Here, we observe a 24-fold plasmonic enhancement, similar to enhancement factors reported in our previous papers for other reaction systems.^{12,40}

$$\text{Quantum efficiency (\%)} = \frac{n \times \text{moles of reduction products}}{\text{moles of photon flux input}} \times 100\% \quad (1)$$

As a control experiment, the CO₂ and H₂O vapor reactants were irradiated without any photocatalyst. Here, no products were detected under 254 or 532 nm wavelength irradiation. In addition, we performed TiO₂ and Au/TiO₂-catalyzed reduction of CO₂ and H₂O at 400 °C without illumination and observed no reaction.

DISCUSSION

To obtain a more rigorous understanding of the mechanism of catalytic enhancement, we perform numerical simulations of the charge and electric potential distributions at the Au

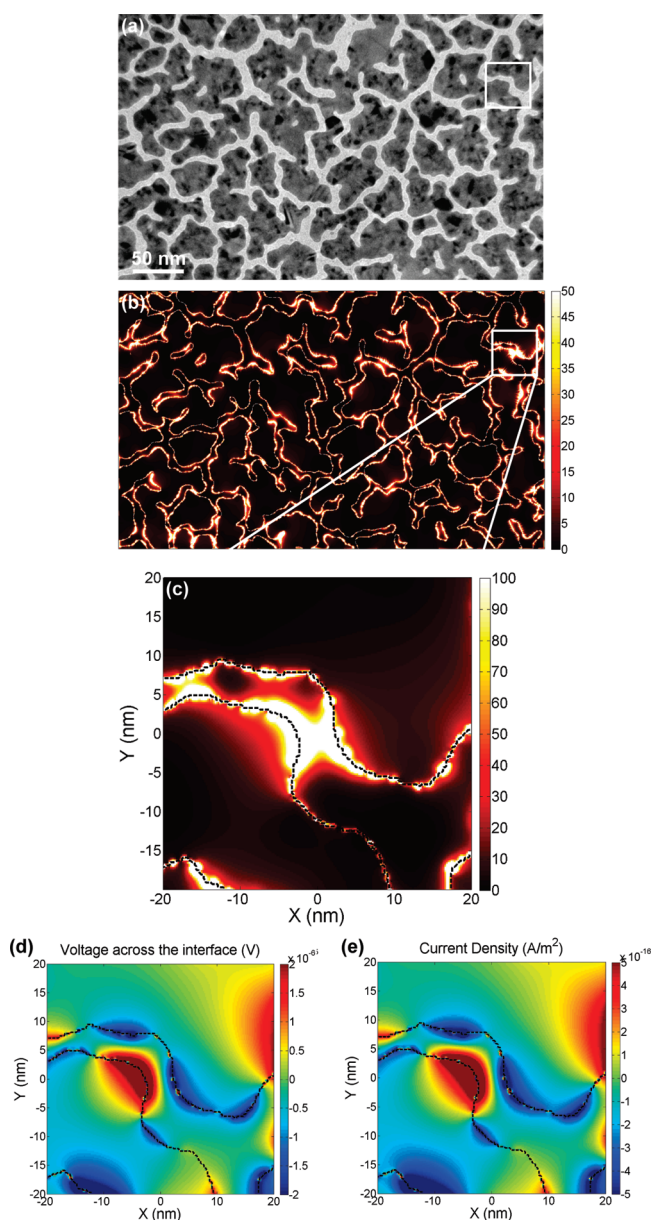


Figure 4. (a) TEM image of a 5 nm thick Au island film deposited on TiO₂. (b–c) Electric field intensity at the interface of Au–TiO₂ calculated using FDTD. (d) Voltage and (e) current density across the Au – TiO₂ interface.

nanoparticle-TiO₂ interface under plasmon resonance excitation, as shown in Figure 4. These simulations are based on the transmission electron microscope (TEM) image of the Au nanoparticle-TiO₂ surface, shown in Figure 4a, which is used to define the spatial extent of the Au nanoparticle islands in our simulation. As discussed in previous publications, the electromagnetic response of the film (Figures 4b and 4c) is dominated by local hot spots where the electric field intensity reaches 1000 times that of the incident electric field at the TiO₂ surface.^{12,40,51,52} This means that the electron–hole pair generation rate is 1000 times that of the incident electromagnetic field. Thus, an increased amount of charge is induced locally in the TiO₂ because of the local field enhancement of the plasmonic nanoparticles. This estimate is based on our electromagnetic simulations, which was in good

agreement with our previous experimental results on water splitting and methyl blue decomposition.^{12,40} While we have no way of measuring the electron–hole pair generation rate in an isolated plasmonic hot spot ($\sim 2 \text{ nm} \times 2 \text{ nm}$), our previous work measuring plasmon-enhanced water splitting provides perhaps the most direct measurement of this,⁴⁰ since every two electrons produce one hydrogen molecule.

In our previous work, we assumed that the observed catalytic enhancement was based purely on the classical electric field enhancement near the metal nanoparticle surfaces, and that no direct transfer of charge was occurring between the plasmonic Au nanoparticles and the TiO₂ semiconductor. However, this mechanism has been discussed widely in previous literature^{14–16,53,54} and is of particular interest for sub-bandgap absorption, providing an alternate mechanism that does not require defects. Here, we explore the possibility of direct electron transfer from the plasmatically excited Au to the adjacent TiO₂ using a thermionic emission model to describe the electron transport across the Schottky barrier, based on the potential differences calculated in the FDTD simulation. By adopting this FDTD-circuit hybrid model, this metal-semiconductor interface should behave like a diode, allowing charge to flow in only one direction. The dielectric function of Au was modeled after the data given in Palik’s handbook.⁵⁵ TiO₂ is modeled as a dielectric with a refractive index of 2.48. The potential difference across the interface is calculated by the formula

$$V = \sum_{\text{interface}} E_z dz \quad (2)$$

where E_z is the z -component of the electric field calculated using the FDTD simulation, and dz is the grid spacing, which in our calculations is 0.2 nm. The current density across the Au nanoparticle-TiO₂ interface is given by the ideal diode equation:

$$J = J_s \left[\exp\left(\frac{eV}{k_B T}\right) - 1 \right] \quad (3)$$

where J_s is the reverse saturation current density given by

$$J_s = \left(\frac{m^* e k_B^2}{2\pi^2 \hbar^3} \right) T^2 \exp\left(-\frac{e\phi_b}{k_B T}\right) \quad (4)$$

Here, m^* is the effective mass of the electron and ϕ_b is the potential barrier across the interface. Figure 4d shows the voltage across the interface, as calculated from our FDTD simulation using eq 2. Figure 4e shows the corresponding electric current density calculated using eq 3. While the equation above clearly indicates diode behavior and suggests a net charge transfer, we can see from the current plot (Figure 4e), that the positive and negative charge transfer (currents) across the interface are equal and, thus, cancel each other. If we integrate the current density over the whole area in the simulation, the net current flow is zero. The reason for this perfect cancelation of positive and negative currents is the very small potential differences across the interface (10^{-5} V), which are well within the ohmic regime of this so-called “diode”.

In the analysis above, we have calculated the electron transfer from the plasmon excitation in the Au nanoparticle to the TiO₂ semiconductor using the voltages calculated from FDTD simulations together with the ideal diode equation for a Au/TiO₂ Schottky junction. We found that there is no net flow of electrons because the Au/TiO₂ junction does not exhibit rectifying behavior at these small voltages. As a result, charge flows in both

directions during each cycle of the plasmon excitation, which cancel each other and produce no net current.

We have calculated the electric fields produced in vacuum and in aqueous solution. The peak local plasmon-induced electric fields are 140 V/m in a H₂O dielectric environment, while in vacuum they are 120 V/m. Therefore, we expect the presence of H₂O molecules to have a minimal effect on the electron–hole pair generation rate. The primary effect of the H₂O environment is to red shift the plasmon resonance wavelength by about 25 nm.

CONCLUSIONS

In summary, we observe plasmonic enhancement of the photocatalytic reduction of CO₂ with H₂O under visible illumination when Au nanoparticles are deposited on top of TiO₂. This enhancement is due to the strong electric fields created by the surface plasmon resonance of the Au nanoparticles, which excite electron–hole pairs locally in the TiO₂ at a rate several orders of magnitude higher than the normal incident light. We demonstrate that the plasmon-excited electrons in the Au nanoparticles cannot transfer directly from the Au to the TiO₂. Only when the photon energy is high enough to excite the d band electrons of Au to a conduction band that lies above the conduction band of TiO₂, does direct charge transfer occur between these two materials. When the incident photon energy is high enough (254 nm UV), an additional mechanism involving the interband electric transitions in Au produces a number of additional photocatalytic reaction products. In this wavelength range, both the excited electrons in Au and TiO₂ contribute to the reduction of CO₂ with H₂O vapor.

ASSOCIATED CONTENT

S Supporting Information. A SEM image of a 5 nm Au thin film after the second annealing, UV–vis, Raman, XRD, XPS spectra, a schematic diagram of the experimental setup, photocatalytic product yields of 5 nm Pt on glass and a Cu foil, and half-reaction equations. This material is available free of charge via the Internet at <http://pubs.acs.org>.

AUTHOR INFORMATION

Corresponding Author

*E-mail: scronin@usc.edu.

Funding Sources

This research was supported in part by AFOSR Award No. FA9550-08-1-00190019 (W.H.H.), ARO Award No. W911NF-09-1-0240 (P.P.), and NSF Award No. CBET-0846725 (W.H.).

ACKNOWLEDGMENT

We thank Prof. G. K. Surya Prakash at the Loker Hydrocarbon Research Institute for help with GC measurements.

REFERENCES

- (1) Inoue, T.; Fujishima, A.; Konishi, S.; Honda, K. *Nature* **1979**, *277* (5698), 637–638.
- (2) Halmann, M. *Nature* **1978**, *275* (5676), 115–116.
- (3) Halmann, M.; Ulman, M.; Aurianblajeni, B. *Solar Energy* **1983**, *31* (4), 429–431.
- (4) Hemminger, J. C.; Carr, R.; Somorjai, G. A. *Chem. Phys. Lett.* **1978**, *57* (1), 100–104.
- (5) Adachi, K.; Ohta, K.; Mizuno, T. *Solar Energy* **1994**, *53* (2), 187–190.
- (6) Anpo, M.; Yamashita, H.; Ichihashi, Y.; Ehara, S. *J. Electroanal. Chem.* **1995**, *396* (1–2), 21–26.
- (7) Wu, J. C. S.; Wu, T. H.; Chu, T. C.; Huang, H. J.; Tsai, D. P. *Top. Catal.* **2008**, *47* (3–4), 131–136.
- (8) Wu, J. C. S.; Lin, H. M.; Lai, C. L. *Appl. Catal., A* **2005**, *296* (2), 194–200.
- (9) Yang, C. C.; Yu, Y. H.; van der Linden, B.; Wu, J. C. S.; Mul, G. *J. Am. Chem. Soc.* **2010**, *132* (24), 8398–8406.
- (10) Koci, K.; Mateju, K.; Obalova, L.; Krejčíková, S.; Lacny, Z.; Placha, D.; Capek, L.; Hospodkova, A.; Solcova, O. *Appl. Catal., B* **2010**, *96* (3–4), 239–244.
- (11) Halmann, M.; Katzir, V.; Borgarello, E.; Kiwi, J. *Sol. Energy Mater.* **1984**, *10* (1), 85–91.
- (12) Hou, W.; Liu, Z.; Pavaskar, P.; Hung, W. H.; Cronin, S. B. *J. Catal.* **2011**, *277*, 149–153.
- (13) Hung, W. H.; Aykol, M.; Valley, D.; Hou, W.; Cronin, S. B. *Nano Lett.* **2010**, *10* (4), 1314–1318.
- (14) Kowalska, E.; Mahaney, O. O. P.; Abe, R.; Ohtani, B. *Phys. Chem. Chem. Phys.* **2010**, *12* (10), 2344–2355.
- (15) Tian, Y.; Tatsuma, T. *Chem. Commun.* **2004**, No. 16, 1810–1811.
- (16) Tian, Y.; Tatsuma, T. *J. Am. Chem. Soc.* **2005**, *127* (20), 7632–7637.
- (17) Wang, X. D.; Caruso, R. A. *J. Mater. Chem.* **2011**, *21* (1), 20–28.
- (18) Yogi, C.; Kojima, K.; Takai, T.; Wada, N. *J. Mater. Sci.* **2009**, *44* (3), 821–827.
- (19) Yogi, C.; Kojima, K.; Wada, N.; Tokumoto, H.; Takai, T.; Mizoguchi, T.; Tamiaki, H. *Thin Solid Films* **2008**, *516* (17), 5881–5884.
- (20) Arabatzis, I. M.; Stergiopoulos, T.; Andreeva, D.; Kitova, S.; Neophytides, S. G.; Falaras, P. *J. Catal.* **2003**, *220* (1), 127–135.
- (21) Tada, H.; Kiyonaga, T.; Naya, S. *Chem. Soc. Rev.* **2009**, *38* (7), 1849–1858.
- (22) Cozzoli, P. D.; Curri, M. L.; Agostiano, A. *Chem. Commun.* **2005**, No. 25, 3186–3188.
- (23) Chen, X.; Zheng, Z. F.; Ke, X. B.; Jaatinen, E.; Xie, T. F.; Wang, D. J.; Guo, C.; Zhao, J. C.; Zhu, H. Y. *Green Chem.* **2010**, *12* (3), 414–419.
- (24) Haruta, M. *Catal. Today* **1997**, *36* (1), 153–166.
- (25) Haruta, M.; Ueda, A.; Tsubota, S.; Sanchez, R. M. T. *Catal. Today* **1996**, *29* (1–4), 443–447.
- (26) Haruta, M.; Tsubota, S.; Kobayashi, T.; Kageyama, H.; Genet, M. J.; Delmon, B. J. *Catal.* **1993**, *144* (1), 175–192.
- (27) Sakurai, H.; Haruta, M. *Appl. Catal., A* **1995**, *127* (1–2), 93–105.
- (28) Sakurai, H.; Ueda, A.; Kobayashi, T.; Haruta, M. *Chem. Commun.* **1997**, No. 3, 271–272.
- (29) Alvarez, M. M.; Khoury, J. T.; Schaaff, T. G.; Shafiqullin, M. N.; Vezmar, I.; Whetten, R. L. *J. Phys. Chem. B* **1997**, *101* (19), 3706–3712.
- (30) Etchegoin, P. G.; Le Ru, E. C.; Meyer, M. *J. Chem. Phys.* **2006**, *125*, (16).
- (31) Glantschnig, K.; Ambrosch-Draxl, C. *New J. Phys.* **2010**, No. 12, 103048.
- (32) Alberius, P. C. A.; Frindell, K. L.; Hayward, R. C.; Kramer, E. J.; Stucky, G. D.; Chmelka, B. F. *Chem. Mater.* **2002**, *14* (8), 3284–3294.
- (33) Corio, P.; Brown, S. D. M.; Marucci, A.; Pimenta, M. A.; Kneipp, K.; Dresselhaus, G.; Dresselhaus, M. S. *Phys. Rev. B* **2000**, *61* (19), 13202–13211.
- (34) Kumar, R.; Zhou, H.; Cronin, S. B. *Appl. Phys. Lett.* **2007**, *91* (22), 223105.
- (35) Chen, K.; Durak, C.; Heflin, J. R.; Robinson, H. D. *Nano Lett.* **2007**, *7* (2), 254–258.
- (36) Kneipp, K. *Phys. Today* **2007**, *60* (11), 40–46.
- (37) Vanduyne, R. P.; Hulstee, J. C.; Treichel, D. A. *J. Chem. Phys.* **1993**, *99* (3), 2101–2115.
- (38) Gratzel, M. *Nature* **2001**, *414* (6861), 338–344.
- (39) Asahi, R.; Morikawa, T.; Ohwaki, T.; Aoki, K.; Taga, Y. *Science* **2001**, *293* (5528), 269–271.

- (40) Liu, Z.; Hou, W.; Pavaskar, P.; Aykol, M.; Cronin, S. B. *Nano Lett.* **2011**, *11*, 1111–1116.
- (41) Li, Q.; Shang, J. K. *Environ. Sci. Technol.* **2009**, *43* (23), 8923–8929.
- (42) Galindo-Hernandez, F.; Gomez, R. J. *Nano Res.* **2009**, *5*, 87–94.
- (43) Zhu, G.; Gavrilenko, V. I.; Noginov, M. A. *J. Chem. Phys.* **2007**, *127*, 10.
- (44) Wang, H.; Tam, F.; Grady, N. K.; Halas, N. J. *J. Phys. Chem. B* **2005**, *109* (39), 18218–18222.
- (45) Cooper, B. R.; Ehrenrei, H.; Philipp, H. R. *Phys. Rev.* **1965**, *138* (2A), A494–A507.
- (46) Johnson, P. B.; Christy, R. W. *Phys. Rev. B* **1972**, *6* (12), 4370–4379.
- (47) Suzer, S.; Ertas, N.; Kumser, S.; Ataman, O. Y. *Appl. Spectrosc.* **1997**, *51* (10), 1537–1539.
- (48) Awate, S. V.; Sahu, R. K.; Kadgaonkar, M. D.; Kumar, R.; Gupta, N. M. *Catal. Today* **2009**, *141* (1–2), 144–151.
- (49) Malwadkar, S. S.; Gholap, R. S.; Awate, S. V.; Korake, P. V.; Chaskar, M. G.; Gupta, N. M. *J. Photochem. Photobiol. A: Chem.* **2009**, *203* (1), 24–31.
- (50) Hung, W. H.; Hsu, I. K.; Bushmaker, A.; Kumar, R.; Theiss, J.; Cronin, S. B. *Nano Lett.* **2008**, *8* (10), 3278–3282.
- (51) Bukasov, R.; Ali, T. A.; Nordlander, P.; Shumaker-Parry, J. S. *ACS Nano* **2010**, *4* (11), 6639–6650.
- (52) Renger, J.; Quidant, R.; van Hulst, N.; Novotny, L. *Phys. Rev. Lett.* **2010**, *104* (4), 046803.
- (53) Ide, Y.; Matsuoka, M.; Ogawa, M. *J. Am. Chem. Soc.* **2010**, *132* (47), 16762–16764.
- (54) Nishijima, Y.; Ueno, K.; Yokota, Y.; Murakoshi, K.; Misawa, H. *J. Phys. Chem. Lett.* **2010**, *1* (13), 2031–2036.
- (55) Palik, E.; Ghosh, G. *Handbook of optical constants of solids: five-volume set*; Academic Press: New York, 1998.